On metalenses with arbitrarily wide field of view

Augusto Martins,[†] Kezheng Li,[‡] Juntao Li,[§] Haowen Liang,[§] Donato Conteduca,[‡] Ben-Hur V. Borges,[†] Thomas F. Krauss[‡] and Emiliano R. Martins[†**]*

[†]São Carlos School of Engineering, Department of Electrical and Computer Engineering, University of São Paulo, Brazil, 13566-590

[‡]University of York, Department of Physics, York, UK, YO10 5DD

[§]State Key Laboratory of Optoelectronic Materials and Technologies, School of Physics, Sun Yat-sen University, Guangzhou, China, 510275

[*]Corresponding author: augusto.martins@usp.br

[**]Corresponding author: erm@usp.br

ABSTRACT: Metalenses are nanostructured surfaces that mimic the functionality of optical elements. Many exciting demonstrations have already been made, e.g. focusing into diffraction-limited spots, or achromatic operation over a wide wavelength range. The key functionality that is yet missing, however, and that is most important for applications such as smartphones or virtual reality, is the ability to perform the imaging function with a single element over a wide field of view. Here, by relaxing the constraint on diffraction limited resolution, we demonstrate the ability of single layer metalenses to perform wide field of view (WFOV) imaging while maintaining high resolution suitable for most applications. We also discuss the WFOV physical properties and in particular, we show that such a WFOV metalens mimics a spherical lens in the limit of infinite radius and infinite refractive index. Finally, we use Fourier analysis to explain the dependence of the FOV on the numerical aperture.

KEYWORDS: dielectric metalens, crystalline silicon, wide field of view metalens, metasurface,

Introduction

Metalenses are an emerging technology that uses nanostructures to modulate the amplitude and phase of an optical beam, thus achieving optical functionalities that can replace or improve bulk optical systems [1-6]. A canonical example for this capability is the development of the hyperbolic metalens, which is free from spherical aberrations [7, 8], a property that is difficult to obtain in bulk optics, especially with single elements. The metalens paradigm, in contrast, can be readily designed to impose a hyperbolic phase profile, thus leading to diffraction limited resolution [6, 8-13]. More interestingly, metalenses can also be designed to realise functionalities that are impossible to achieve in bulk optics. We exploit this new degree of freedom for metalens design by addressing the problem of field of view (FOV), which has not received much attention so far. Indeed, in many applications, such as imaging systems, FOV is the crucial parameter, but metalens designs that have been put forward to date are limited to procedures that reduce off-axis aberration via numerical optimisation [14], often combined with a doublet system [15, 16]. While ingenious, these approaches are limited to moderate Numerical Apertures (NA) and do not explore the physical mechanisms limiting the FOV. An alternative strategy is to relax the requirement of diffraction limited resolution in order to achieve a wide FOV (WFOV) in a singlet system[17-19]. Here, we demonstrate WFOV imaging with a single layer metalens-with an NA of 0.8. We show that the Point Spread Function (PSF) shape remains undistorted inside an angular cone > 170°. The design trades off FOV against the diffraction limited resolution equivalent to an NA of 0.27, which is however sufficient for most imaging applications, including smartphones. We discuss the physical properties of the WFOV metalens and, using Fourier analysis, we show that the WFOV metalens achieves an arbitrarily large FOV by mimicking a bulk spherical lens with infinite refractive index and infinite radius of curvature. The WFOV is therefore unique in that its bulk counterpart is

impossible to obtain. Finally, we compare the WFOV metalens to the diffraction limited (DL) hyperbolic metalens, showing that they are complementary in the sense that the FOV of the former and the resolution of the latter improve monotonically with the NA.

2. Design

The DL and WFOV metalenses employ a hyperbolic (Equation 1) and a quadratic (Equation 2) phase profiles, respectively. DL metalenses with hyperbolic phase profiles were first demonstrated by [20]. Since their properties are well known in the literature [4, 6, 8-11, 20-22], we focus attention on the description of the quadratic phase profile.

$$\phi_{hyp}(r) = -k_0 n_{ext}\left(\sqrt{f^2 + r^2} - f\right) \tag{1}$$

$$\phi_{quad}(r) = \frac{-k_0 r^2}{2f} n_{ext} \tag{2}$$

A quadratic phase profile for WFOV metalenses was first proposed by Pu et.al [17]. As shown by the authors, WFOV is achieved because the quadratic phase profile translates a linear phase (imposed by a plane wave at oblique incidence) into a spatial shift, as shown in Equation 3 below. As a result, the effect of oblique incidence is a spatial translation of the focal spot.

$$\phi(r) = -\frac{k_0}{2f}(x^2 + y^2) - k_0 x \sin\theta = -\frac{k_0}{2f}[(x + f\sin\theta)^2 + y^2] + \frac{f k_0 \sin^2\theta}{2} \tag{3}$$

The quadratic metalens achieves a WFOV but it introduces spherical aberrations, which limits the resolution. As shown in [17], the resolution limitation can be understood in terms of an effective aperture of the metalens, outside of which the phase modulation is so rapid that diffraction orders become evanescent. The resolution of the quadratic metalenses, however, is sufficiently high for most imaging applications, as we show in the next section. Further insights into the physics of quadratic phase-profile lenses are provided in the following sections. A key remaining challenge

not addressed by [17] is wide field of view imaging in the visible wavelength range, which we demonstrate here.

Experimental demonstration

The metalenses are realised using an array of 230 *nm* tall c-Si posts on a sapphire substrate [21, 22] as shown in Figure 1a. Following the usual procedure, the metasurface is constructed from the transmission/phase maps of periodic arrays of c-Si posts (Figure 1b). The period of the arrays a is fixed and define the size of the meta-atoms, which in our design is a =190 *nm*. Each array has a different diameter of the c-Si posts, and their transmission and phase were calculated using the Rigorous Coupled Wave Analysis (RCWA)[23, 24]. The resulting transmission and phase of each array are then combined to generate the phase map (Figure 1b). The desired phase profile is then discretised using the phase map. All metasurfaces shown here use 8 different phase levels, which are marked with circles in Figure 1b. More details are provided in the Supporting Information (SI), Section S1 including the angle-dependent phase maps.

Micrographs of the metasurfaces are shown in Figure 1c-d, highlighting the excellent fabrication quality despite the very small period of 190 *nm* (see materials and methods, for details on fabrication and the imaging system, and section S2 of the SI for more micrographs). A picture of the metalens on a ruler is shown in Figure 1e. The imaging system (Figure 1f) integrates the metalens with a complementary metal oxide semiconductor (CMOS) sensor (Sony IMX219) in a 3D printed box. We fabricated two metalenses: a WFOV using a quadratic profile [17-19], and a diffraction limited (DL) metalens using a hyperbolic profile as a reference. The role of the phase profiles is discussed in the next section.

The performance of the WFOV lens is shown in Figure 2a, in comparison to a DL design (Figure 2b) using a USAF 1964 chart. The USAF chart is shown in Figure 2c, highlighting the field of

view zones. The metalenses have the same numerical aperture of NA = 0.8 which is here defined as $D/\sqrt{D^2+4f^2}$, where D and f are the lens aperture diameter and focal length, respectively. For all lenses, we use a focal length of $f = 750\ \mu m$ and a diameter of $D = 2$ mm. It is clear that the image obtained with the WFOV metalens is virtually free of aberrations, except for the barrel distortion or "fish-eye" effect, which is typical of optical systems with a wide field of view[15]. The barrel distortion arises due to a mismatch between the actual displacement of the focal spot (which depends on the sine of the angle of incidence), and the paraxial displacement (which depends on the tangent of the angle). The measured displacements are shown in Figure 2d. Because this displacement is predictable, it can be corrected in post-processing [25], so it does not constitute a fundamental limitation of the lens.

The image of the DL metalens, in contrast, is strongly blurred by off-axis aberrations. The only area where the DL lens achieves superior performance is the very centre of the image. The extremely large FOV of the WFOV metalens is demonstrated by analysing the Point Spread Function (PSF) shown in Figure 3a-b for different angles of incidence (see the materials and methods section for details on the measurement setup). The normalized PSF of the WFOV metalens is virtually unchanged for an incoming angle as high as 89° (Figure 3a), while the normalized PSF of the DL lens is already badly distorted for an angle of only 2° (Figure 3b). The focusing efficiency of the WFOV metalens is virtually unchanged up to an angle of incidence of 20 degrees, and reduces for higher angles due to a reduction in the transmission efficiency. A more detailed analysis of the efficiency is shown in the end of this section. The angular dependence of the PSF's full width at half maximum (FWHM) in the x-direction in Figure 3a-b is shown in Figure 3c, comparing experimental and theoretical values (see SI for details on how the PSF is calculated). For perpendicular incidence (0°), the DL lens has a diffraction limited FWHM, which explains its

high performance at the very centre of the image, while the FWHM of the WFOV lens is twice as large (we notice in Figure 3c that the measured FWHM of the DL lens is larger than the theoretical, which we attribute mainly to the objective used in the imaging of the PSF – see SI for more details). The FWHM of the DL lens, however, rapidly increases for small angles of incidence, while the FWHM of the WFOV lens is constant up to angles as high as ±89°.

We notice that our WFOV single layer metalens achieves a FOV > 170° (characterised by the PSF measurements) and a FWHM ~ $2\lambda_0$, which is comparable to bulk optics WFOV lenses. For example, the wide and ultra-wide lenses of the iPhone 11 Pro Max have a FOV = 60°, FWHM ~ $1.87\lambda_0$ and a FOV = 120°, FWHM ~ $2.26\lambda_0$, respectively [26, 27]. As another example, the Nikkon AS-Fisheye NIKKOR 8-15mm f/3.5-4.5E ED system has a FOV = 60°, and FWHM ~ $3.54\lambda_0$.

The angle dependent focusing and transmission efficiencies of the quadratic and hyperbolic metalenses are shown in Figure 4a (quadratic) and Figure 4b (hyperbolic) for both s (black lines) and p (blue lines) polarizations. The theoretical efficiencies, determined by numerical simulations, are shown in Figure S10 of the SI, section S10. The focusing efficiencies were determined by integration of the energy in the focal spot using a circular aperture with a radius of 7.5 μm. The dotted lines show the transmission efficiencies. To better assess the metalens performance, the experimental focusing efficiency with respect to both incident (solid lines) and transmitted power (dashed lines) are shown in Figure 4. Comparing these two efficiencies is helpful to determine whether a reduction in the focusing efficiency comes from a loss of the metalens ability to focus light, or from a loss of the transmitted power itself. We thus conclude that the reduction of the focusing efficiency with respect to the incoming power (Figure 4a, solid lines) is not due to a loss of ability to focus light, but it is rather due to a loss of transmitted power itself (Figure 4a, dotted lines), which is mostly due to the cosine dependent projected area. Nevertheless, the efficiency

with respect to incoming power (Figure 4a, solid lines) is virtually unchanged up to an angle of 20°.

As expected, the efficiencies of the quadratic lens are more tolerant at oblique incidence than the efficiencies of the hyperbolic lenses. Notice, however, that the efficiencies of the quadratic lens (3.5% for focusing with respect to incoming power and 14% for transmission) are much lower than the efficiencies of the hyperbolic lens (23% for focusing with respect to incoming power and 31% for transmission). This is an intrinsic consequence of a combination of spherical aberrations and the effective numerical aperture of the quadratic lens[17], (for a more detailed analysis, see SI – Section S3). This feature highlights the need of using low loss materials, such as c-Si, in the design of WFOV metalenses. Notice that the simulated focusing efficiency (shown in Figure S10a, solid lines) is -13 dB, (i.e., 5%), as compared to the -14.5 dB (i.e., 3.5%) of the experimental efficiency (Figure 4a, solid lines). We therefore achieve an experimental focusing efficiency of 3.5/5*100% = 70% compared to the simulated efficiency.

Relationship with bulk optics and role of phase profile

In order to understand how the physics of the WFOV metalens relates to bulk optics and how it achieves an arbitrarily large FOV, consider a conventional spherical lens with light incident at oblique incidence at some angle $\theta = 30°$, as shown in Figure 5a for a conventional lens with $R = 500\ \mu m$ and $f = 500\ \mu m$ (ray tracing obtained using Comsol). The focal distance f of the spherical lens is given by the ratio of the radius of curvature R and the refractive index contrast Δn between the lens and the surrounding medium ($f = R/(2\Delta n)$). It is obvious from the equation that the same focal length can be achieved by keeping the ratio of radius and index contrast constant. Conventional optical systems are constrained to index contrasts of typically $\Delta n < 1$ by the availability of suitable materials, so this ratio is not explored in practise. Metalenses do not have

this constraint, however, and they can be designed to mimic large radii and high refractive indices. This opportunity is explored in Figure 5. For example, Figure 5b shows the example of a lens with twice the radius and twice the index contrast (R = 1000 μm, Δn = 1) of the conventional lens. Note that the ray convergence is already improved compared to the lens of Figure 5a. The convergence then improves further as the radius of curvature is increased while keeping the focal length constant, as illustrated in Figure 5c, for which R = 1500 μm, Δn = 1.5.

This improvement of convergence with increasing radius and refractive index can be readily understood via the Fourier Transform (FT) of the field distribution immediately after the lens for perpendicular incidence (Figure 5d), i.e. by considering k-space. The FT of the large radius lens (Figure 5d - blue line) is flatter than that of the conventional lens (Figure 5d - black line), which increases the symmetry of the Fourier components (see sections S4 and S5 on the SI for more details). Symmetry in k-space is important because it ensures that the rays contributing to image formation from opposite sides of the lens have equal strength, thus forming a well-defined spot. For oblique incidence (Figure 5e), this symmetry is compromised, unless the FT is flat, which is the case for large radius spherical lenses (see also Figure 6a-b). Note that the asymmetry in k-space is particularly pronounced for the hyperbolic lens, which explains its very limited field of view [4].

These insights clarify the optical performance of the WFOV lens. Indeed, the quadratic profile is obtained in the limit of both R and Δn going to infinity while keeping $f = R/2\Delta$n constant, as shown in Equation 4 (see materials and methods and section S6 on the SI for more details on the phase profiles).

$$\phi(r) = \lim_{\substack{(R,\Delta n)\to(+\infty,+\infty) \\ f\ const.}} -\frac{4\pi}{\lambda_0} n_{ext} \Delta n \left(R - \sqrt{R^2 + r^2} \right) = -\frac{\pi r^2}{\lambda_0 f} n_{ext} \tag{4}$$

Where n_{ext} is the refractive index of the focusing medium, λ_0 and r are the free space wavelength and the distance to the metalens' centre, respectively. Since a metalens with quadratic profile corresponds to the limit of a spherical lens with infinite radius and infinite refractive index, we conclude that the WFOV metalens does not have a bulk counterpart. We notice that a bulk lens with quadratic profile is not equivalent to the WFOV lens, since their optical characteristics coincide only for paraxial rays (see SI for a comparison between the metalens and the bulk lens).

Fourier analysis of the FOV and relationship with hyperbolic metalenses

The FT of the WFOV lens is further explored in Figure 6a for NAs of 0.4 (black line), 0.65 (blue line) and 0.9 (red line). Notice that, the larger the NA, the wider the FT. In fact, for an NA ≈ 0.9 the FT covers the range of normalized k vectors from -2 to 2, i.e., it covers a region twice as large as the light line, which makes the FT invariant for oblique incidence (Figure 6b), thus resulting in a FOV = 180°. We note an interesting difference of lens performance on NA; for most lens designs, including the hyperbolic design, it is the spatial resolution which increases with increasing NA. For the WFOV lens, however, it is the FOV that increases with increasing NA. This interesting behaviour is explored in Figure 6c-d. As expected, the FWHM of the DL (hyperbolic) lens (Figure 6c – black line) decreases monotonically as the NA increases, while the FWHM for the spherical (blue line) and WFOV (red line) lenses remain constant beyond an NA of 0.2 (spherical) and ≈ 0.3 (WFOV). The FTs of the WFOV and DL lenses are very similar up to an NA ≈ 0.3 (see section S4 on the SI for the Fourier Transform profiles), and consequently their FWHM are identical in the low NA regime; for higher NAs, however, their FTs differ, which is a manifestation of spherical aberrations and limits the FWHM of the WFOV lens.

In terms of field of view, however, the roles are reversed. The FOV of the DL lens now rapidly decreases as the DL increases (Figure 6d – black line – see section S7 on the SI for detailed information on how the FOV is quantified), while the FOV of the WFOV lens (red line) increases

monotonically with NA, until it reaches 180° for NA ≈ 180°. Note that the FOV of the spherical lens (blue line) saturates at a value of ≈ 20°. This limitation of the spherical lens highlights the unique advantage of the WFOV design: even though the WFOV lens is fundamentally based on the spherical design, it achieves much higher performance by going to the $R,n \rightarrow +\infty$ limit. Therefore, while the spatial resolution of the DL lens increases with NA (at the expense of FOV), it is the FOV that increases with NA for the WFOV lens. We note, however, that the spatial resolution of the WFOV lens can be readily improved by using oil immersion, while the limited FOV of the DL lens can only be improved with a suitable phase corrector, e.g. in a doublet configuration [15, 16].

Discussion

In conclusion, we demonstrate WFOV imaging with a single layer metalens by relaxing the constraint on diffraction limited resolution; in particular, we show that WFOV metalenses mimic a spherical lens in the limit of infinite radius of curvature and infinite refractive index. This metalens has an arbitrarily large FOV and can be seen as complementary to the established DL (hyperbolic) lens design, in the sense that the FOV of the WFOV lens increases with the NA, while it is the resolution which increases with NA in DL lenses. We note that the WFOV metalens achieves a FWHM ≈ $2\lambda_0$ which is sufficient for all but the most demanding imaging applications, including the very best smartphone cameras which have a maximum NA of ~ 0.3 (notice that FWHM ≈ $2\lambda_0$ is obtained in the DL lens with NA = 0.27). The WFOV metalens opens up an unprecedented degree of freedom to control the FOV, with achromatic operation presenting the next challenge. Overall, we believe that the WFOV metalens will make an important contribution to the development of novel wide-field and high-resolution imaging applications, including smartphone imaging, virtual reality viewers and miniaturised high-end scientific imaging systems.

Methods

Fabrication: The metalenses were fabricated on commercially available 230 nm thick c-Si (100) wafers epitaxially grown on a sapphire substrate (from The Roditi International Corporation Limited.). The sample was cleaned using acetone, isopropyl alcohol (IPA) and oxygen plasma. It was subsequently spin-coated with a 300 nm positive electron beam resist layer (AR-P 6200.13, AllResist GmbH) followed by a 60 nm charge dissipation layer (AR-PC 5090, AllResist GmbH). The structure was then patterned using an e-beam system (Voyager, Raith GmbH) followed by a resist development in xylene for 2 minutes. The pattern was transferred to silicon using reactive ion etching. SEM micrographs of finished metalenses are shown in Figure S5a-f on section S2 of the SI.

Camera (imaging system): The metalens was integrated with a CMOS sensor (Sony IMX219 8-megapixel sensor) to form a metalens camera. The camera set-up is shown in Figure S6a-c on section S2 of the SI. Figure S6a shows a schematic of the metalens position with respect to the CMOS sensor, where the red arrow indicates that the CMOS position is adjustable to focus the image. Figure S6b-c shows the integrated system without and with the lid on, respectively. The imaging system uses a monochromatic light source, as indicated in Figure S6d. In order to better show the FOV, parts of the image were magnified with the system shown in Figure S6e. The set-ups of Figure S6d-e were then used to record the images shown in Figure S8a-b, respectively. The images obtained with the WFOV and DL metalenses are shown in Figure S8a-b, respectively. The areas indicated by the squares were magnified and shown in Figure S8b-d.

Point Spread Function (PSF) characterization setup: The PSFs were measured using a rotation stage, as shown in Figure S9. The metalens was illuminated by a laser at a wavelength of 532 nm, and the corresponding PSFs were then imaged onto the CMOS sensor.

Lenses phase profiles: The lenses' phase profiles are defined on Table S3 with the pertinent parameters defined at Table S4 in section S7 of the SI.

Notice that the limit of the spherical lens when the radius and refractive index go to infinity, keeping the focal length fixed, is given by a quadratic profile. One might then think that the WFOV lens behaves just like a bulk lens with a quadratic profile. We emphasise that this is not the case, however, because their behaviour is only equivalent for paraxial rays, as illustrated in Figure S13, which shows a ray tracing comparison between the WFOV metalens (left) and quadratic bulk lens (right).

Notice that the WFOV metalens, for being flat, focuses light at the same distance (750 μm), irrespective of the angle of incidence. The focal point of the bulk quadratic lens, in contrast, is dependent of the angle of incidence (which is a manifestation of Petzval curvature aberration). This effect is highlighted by comparing the blue dashed line in Figure S13d-e, that marks the focal point for different angles of incidence, with the red dashed line that marks the focal distance at normal incidence. Notice how the focal length of the bulk lens increases at oblique incidence, tracing the Petzval field curvature.

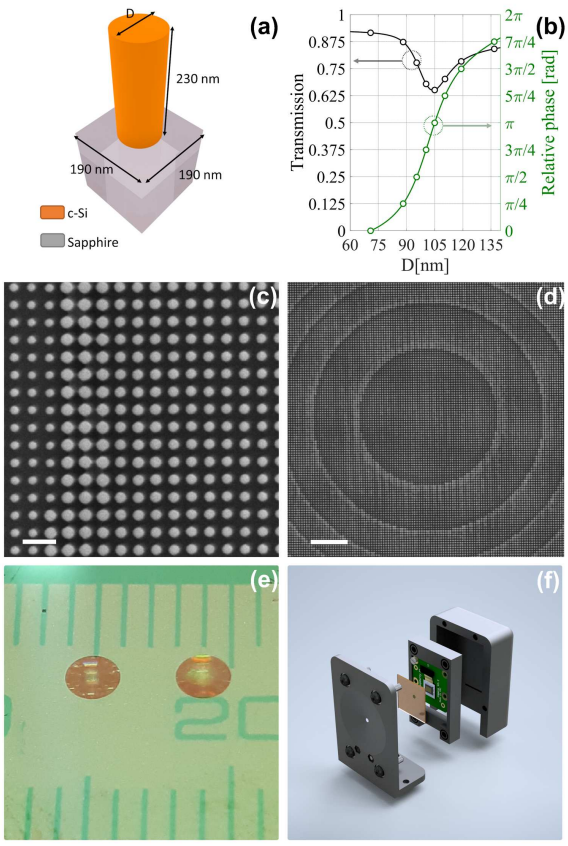

Figure 1. (a) Meta-atom representation and (b) transmission and phase maps. D is the diameter of the c-Si posts, and the circles mark the eight phase levels used to encode the metalens (the diameters are shown in section S1 on the SI). The operating wavelength is 532 *nm*. (c) and (d) show SEM micrographs of the array of c-Si nanoposts forming the metalens. The scale bars are 400 *nm* (c) and 3 *μm* (d). (e) photograph of the fabricated metalenses. The ruler's units are in *mm* indicating the 2 mm diameter. (f) Setup of the 3D-printed system integrating the metalens with a CCD camera.

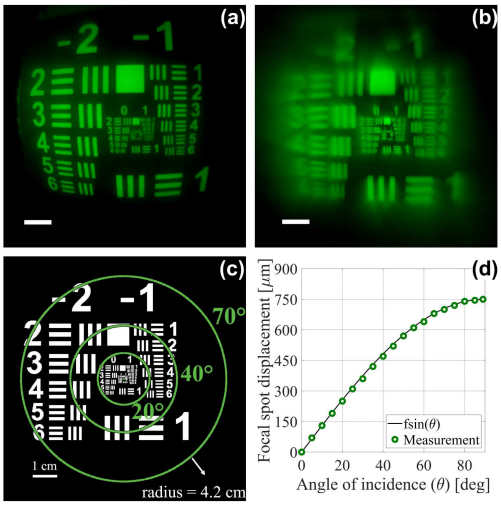

Figure 2. (a) Image of a USAF 1964 chart obtained with the WFOV (quadratic) metalens using the setup of Fig. 1 (f); the scale bar is 100 μm long. (b) Image of a USAF 1964 chart obtained with the DL (hyperbolic) metalens using the setup of Fig. 1 (f); the scale bar is 100 μm. The distance between the lens and the object is 6 cm. (c) Picture of the USAF 1964 chart with the field of view zones highlighted by dashed circles. The field of view zones marked by the solid circles (from innermost to outermost) are 20°, 40° and 70°. The radius of the outermost circle is 4.2 cm. See SI, section S2 for an image with a wider field of view (d) Focal spot displacement as function of the incident angle. The continuous line shows the product of the sine function with the focal length.

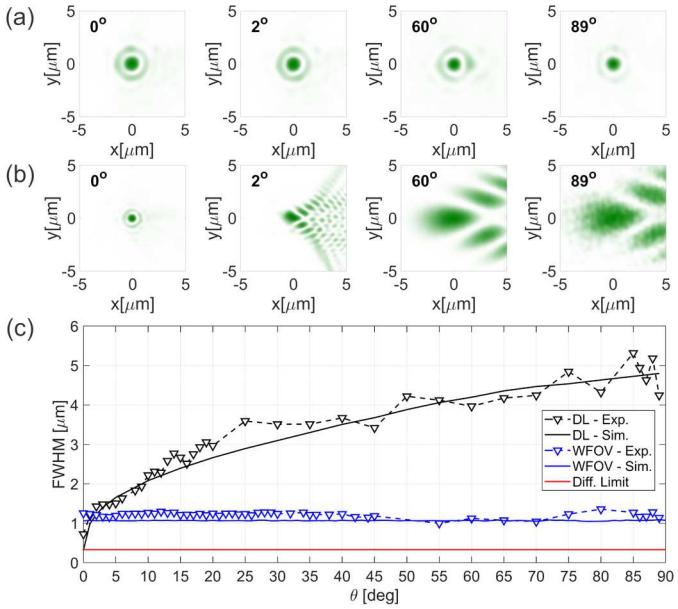

Figure 3. PSFs for different angles of incidence for the WFOV (a) and the DL (b) metalenses. The x axis in (a) and (b) is centred at the maximum of each PSF. (c) Dependence of the FWHM on the angle of incidence for both lenses. Focal length is 750 μm, diameter is 2 mm, operating wavelength is 532 nm and the NA=0.8.

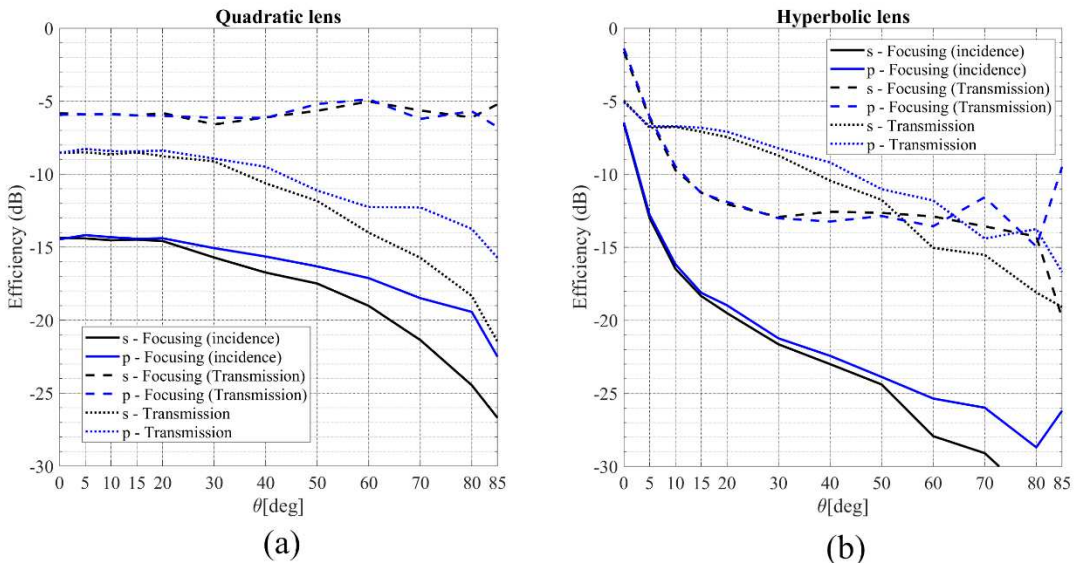

Figure 4. Measured transmission (dotted lines) and focusing efficiencies (dashed and solid lines) as a function of angle the of incidence for both s and p polarisations. The focusing efficiency is determined with respect to both incoming power (solid lines) and transmission power (dashed lines). (a) efficiencies of the quadratic metalens. At perpendicular incidence, the transmission efficiency is 14%, the focusing efficiency with respect to incoming power is 3.5% and the focusing efficiency with respect to transmitted power is 25%. (b) efficiencies of the hyperbolic metalens. At perpendicular incidence, the transmission efficiency is 31%, the focusing efficiency with respect to incoming power is 23%, and the focusing efficiency with respect to transmitted power is 74%.

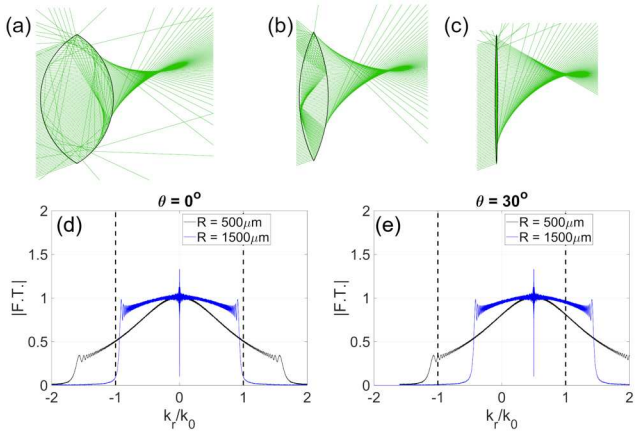

Figure 5. Comparison between the WFOV metalens and spherical bulk lens. Ray traces for a spherical bulk lens (NA=0.65) for oblique incidence (θ=30°) and a radius of curvature of (a) 500 μm, (b) 1000 μm, and (c) 1500 μm. (d) FT amplitude of the field generated by the spherical lenses in (a) (black line) and (c) (blue line); the FT in (d) is for perpendicular incidence and (e) for oblique incidence (θ=30°).

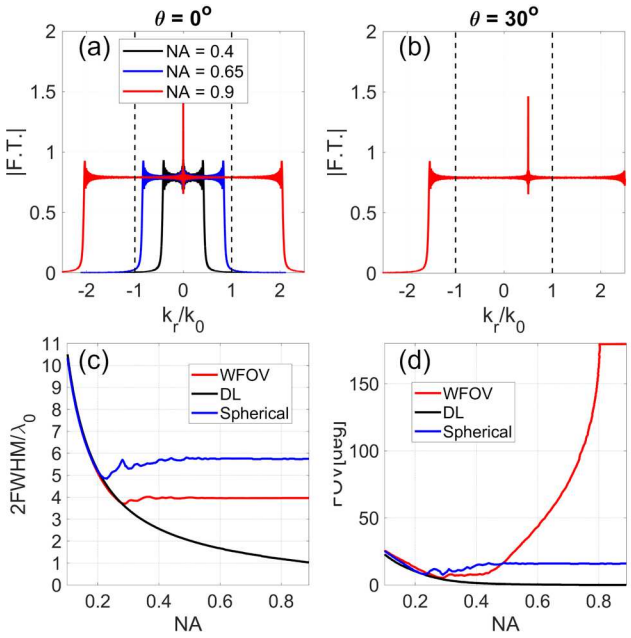

Figure 6. (a) Fourier Transforms of the WFOV lens for an NA of 0.4 (black), 0.65 (blue) and 0.9 (red), for perpendicular incidence. (b) same as red line in (a), but for oblique incidence. (c) Spatial resolution ($2FWHM/\lambda_0$) and (d) FOV as a function of NA for the DL (black), spherical (blue) and WFOV (red) metalenses. The operating wavelength is 532 *nm* and focal length is 500 μm for all cases.

AUTHOR INFORMATION

Corresponding Author

*Corresponding author: augusto.martins@usp.br

**Corresponding author: erm@usp.br

Author Contributions

AM, TFK and ERM conceived the idea of the paper. JL, HL and BVB contributed in the analysis of results and design of the experiments. AM did all the calculations and most of the experiments. KL and DC contributed to the fabrication and optical characterization. TFK and ERM supervised the project and wrote the manuscript.

ACKNOWLEDGMENT

This work is supported by São Paulo Research Foundation (FAPESP) (Grants 2013/07276-1, 2015/21455-1, 2020/00619-4 and 2018/25372-1); National Council for Scientific and Technological Development (CNPq) (303562/2017-2); National Natural Science Foundation of China (11534017, 11761131001, 11974436, 11704421, 91750207); The Key R&D Program of Guangdong Province (2018B030329001, 2019B010152001); Guangzhou Science and Technology Project (201805010004); Natural Science Foundation of Guangdong Province (2020B1515020019, 2020A1515011184); The Fundamental Research Funds for the Central Universities. The authors acknowledge financial support by the EPSRC of the UK (Grants EP/P02324X/1 and EP/P030017/1). Prof Thomas F Krauss acknowledges a Royal Society Wolfson Merit Award.

ASSOCIATED CONTENT

Supporting Information.

Suporting information: Phase and transmission maps, SEM micrographs, optical setups, additional imaging comparison between WFOV and DL metalenses. Additional information on Metalens focusing and transmission efficiencies. Fourier Transforms of quadratic (WFOV) and hyperbolic (DL) field profiles. Spectrum flattening of the spherical phase profile Comparison between the WFOV metalens and an equivalent bulk quadratic lens at different angles, phase profile equations. FOV characterization. Angular spectrum formalism (PDF). This material is available free of charge via the Internet at http://pubs.acs.org

ABBREVIATIONS

WFOV wide field of view; FOV field of view; NA numerical aperture; DL diffraction limited; CMOS complementary metal oxide semiconductor; FWHM full width at half maximum; PSF point spread function.

REFERENCES

(1) Genevet, P.; Capasso, F.; Aieta, F.; Khorasaninejad, M.; Devlin, R., Recent advances in planar optics: from plasmonic to dielectric metasurfaces. Optica 2017, 4 (1), 139-152.

(2) Yu, N.; Capasso, F., Flat optics with designer metasurfaces. Nature Materials 2014, 13, 139-150.

(3) Kildishev, A. V.; Boltasseva, A.; Shalaev, V. M., Planar Photonics with Metasurfaces. Science 2013, 339, 1232009.

(4) Liang, H.; Martins, A.; Borges, B.-H. V.; Zhou, J.; Martins, E. R.; Li, J.; Krauss, T. F., High performance metalenses: numerical aperture, aberrations, chromaticity, and trade-offs. Optica 2019, 6 (12), 1461-1470.

(5) Rubin, N. A.; D'Aversa, G.; Chevalier, P.; Shi, Z.; Chen, W. T.; Capasso, F., Matrix Fourier optics enables a compact full-Stokes polarization camera. Science 2019, 365 (6448), eaax1839.

(6) Khorasaninejad, M.; Capasso, F., Metalenses: Versatile multifunctional photonic components. Science 2017, 358 (6367), eaam8100.

(7) Aieta, F.; Genevet, P.; Kats, M.; Capasso, F., Aberrations of flat lenses and aplanatic metasurfaces. Opt. Express 2013, 21 (25), 31530-31539.

(8) Paniagua-Domínguez, R.; Yu, Y. F.; Khaidarov, E.; Choi, S.; Leong, V.; Bakker, R. M.; Liang, X.; Fu, Y. H.; Valuckas, V.; Krivitsky, L. A.; Kuznetsov, A. I., A Metalens with a Near-Unity Numerical Aperture. Nano Letters 2018, 18 (3), 2124-2132.

(9) Khorasaninejad, M.; Chen, W. T.; Devlin, R. C.; Oh, J.; Zhu, A. Y.; Capasso, F., Metalenses at visible wavelengths: Diffraction-limited focusing and subwavelength resolution imaging. Science 2016, 352 (6290), 1190-1194.

(10) Lalanne, P.; Chavel, P., Metalenses at visible wavelengths: past, present, perspectives. Laser & Photonics Reviews 2017, 11 (3), 1600295.

(11) Liang, H.; Lin, Q.; Xie, X.; Sun, Q.; Wang, Y.; Zhou, L.; Liu, L.; Yu, X.; Zhou, J.; Krauss, T. F.; Li, J., Ultrahigh Numerical Aperture Metalens at Visible Wavelengths. Nano Letters 2018, 18 (7), 4460-4466.

(12) Arbabi, A.; Horie, Y.; Ball, A. J.; Bagheri, M.; Faraon, A., Subwavelength-thick lenses with high numerical apertures and large efficiency based on high-contrast transmitarrays. Nature Communications 2015, 6, 7069.

(13) Chen, W. T.; Zhu, A. Y.; Khorasaninejad, M.; Shi, Z.; Sanjeev, V.; Capasso, F., Immersion meta-lenses at visible wavelengths for nanoscale imaging. Nano letters 2017, 17 (5), 3188-3194.

(14) Kalvach, A.; Szabó, Z., Aberration-free flat lens design for a wide range of incident angles. JOSA B 2016, 33 (2), A66-A71.

(15) Arbabi, A.; Arbabi, E.; Kamali, S. M.; Horie, Y.; Han, S.; Faraon, A., Miniature optical planar camera based on a wide-angle metasurface doublet corrected for monochromatic aberrations. Nature Communications 2016, 7, 13682.

(16) Groever, B.; Chen, W. T.; Capasso, F., Meta-Lens Doublet in the Visible Region. Nano Letters 2017, 17 (8), 4902-4907.

(17) Pu, M.; Li, X.; Guo, Y.; Ma, X.; Luo, X., Nanoapertures with ordered rotations: symmetry transformation and wide-angle flat lensing. Opt. Express 2017, 25 (25), 31471-31477.

(18) Guo, Y.; Ma, X.; Pu, M.; Li, X.; Zhao, Z.; Luo, X., Ultrathin Metalenses: High-Efficiency and Wide-Angle Beam Steering Based on Catenary Optical Fields in Ultrathin Metalens (Advanced Optical Materials 19/2018). Advanced Optical Materials 2018, 6 (19), 1870073.

(19) Engelberg, J.; Zhou, C.; Mazurski, N.; Bar-David, J.; Kristensen, A.; Levy, U., Near-IR wide-field-of-view Huygens metalens for outdoor imaging applications. Nanophotonics 2020, 9 (2), 361-370.

(20) Aieta, F.; Genevet, P.; Kats, M. A.; Yu , N.; Blanchard, R.; Gaburro, Z.; Capasso, F., Aberration-Free Ultrathin Flat Lenses and Axicons at Telecom Wavelengths Based on Plasmonic Metasurfaces. Nano Letters 2012, 12, 4932-4936.

(21) Zhou, Z.; Li, J.; Su, R.; Yao, B.; Fang, H.; Li, K.; Zhou, L.; Liu, J.; Stellinga, D.; Reardon, C. P.; Krauss, T. F.; Wang, X., Efficient Silicon Metasurfaces for Visible Light. ACS Photonics 2017, 4 (3), 544–551.

(22) Martins, A.; Li, J.; da Mota, A. F.; Wang, Y.; Neto, L. G.; do Carmo, J. P.; Teixeira, F. L.; Martins, E. R.; Borges, B. V., Highly efficient holograms based on c-Si metasurfaces in the visible range. Opt Express 2018, 26 (8), 9573-9583.

(23) Whittaker, D. M.; Culshaw, I. S., Scattering-matrix treatment of patterned multilayer photonic structures. Physical Review B 1999, 60 (4), 2610–2618.

(24) Popov, E.; Nevière, M., Maxwell equations in Fourier space: fast-converging formulation for diffraction by arbitrary shaped, periodic, anisotropic media. Journal of the Optical Society of America A 2001, 18 (11), 2886-2894.

(25) Lee, M.; Kim, H.; Paik, J., Correction of barrel distortion in fisheye lens images using image-based estimation of distortion parameters. IEEE ACCESS 2019, 7, 45723-45733.

(26) GSM Arena - iPhone 11 Pro - Technical Specifications. https://www.gsmarena.com/apple_iphone_11_pro_max-9846.php (accessed Jan 20, 2020).

(27) Apple iPhone 11 Pro - Technical Specifications. https://www.apple.com/iphone-11-pro/specs/ (accessed Jan 20, 2020).

For table of Contents Use Only

Manuscript title: On metalenses with arbitrarily wide field of view

Authors: Augusto Martins, Kezheng Li, Juntao Li,[§]Haowen Liang, Donato Conteduca, Ben-Hur V. Borges, Thomas F. Krauss and Emiliano R. Martins

Synopsis: Wide field of view metalens design as the limit of a bulk lens with infinite radius of curvature and refractive index.